Rare Met. (2023) 42(6):1800–1807
https://doi.org/10.1007/s12598-022-02247-z

RARE METALS

LETTER

Three-dimensional ordered porous N-doped carbon-supported accessible Ni-N_x active sites for efficient CO_2 electroreduction

Si-Jia Zheng, Hua Cheng*, Jin Yu, Qin Bie, Jing-Dong Chen, Feng Wang, Rui Wu, Daniel John Blackwood, Jun-Song Chen*

Received: 10 July 2022 / Revised: 25 October 2022 / Accepted: 15 November 2022 / Published online: 21 March 2023

Electrocatalytic reduction of carbon dioxide (CO_2RR) into high value-added chemicals and fuels has been regarded as a promising approach to achieve carbon neutrality. Though nickel-nitrogen-carbon (Ni-N-C) electrocatalysts have shown superior CO_2RR performance, the synthesis of highly effective Ni-N-C catalyst is still challenging. Herein, a three-dimensional (3D) ordered porous nitrogen-doped carbon-supported Ni-N_x catalyst has been synthesized by direct pyrolysis of a mixture of SiO_2, polyvinyl pyrrolidone, nickel-phenanthroline complex, followed by the removal of the SiO_2 templates. Benefiting from the porous structure and accessible active sites, the optimized catalyst exhibits a high CO Faradaic efficiency above 85% between –0.6 and –0.9 V versus reversible hydrogen electrode (vs. RHE), and a large CO current density (j_{CO}) of –16.2 mA·cm^{-2} at –0.8 V (vs. RHE). Density functional theory (DFT) calculations demonstrate that the Ni-N-C catalyst with Ni-N_x species can enhance CO_2RR reaction dynamic process and suppress hydrogen evolution reaction, thus improving the conversion efficiency toward CO_2RR.

Electrocatalytic reduction of carbon dioxide (CO_2RR) into commercial chemicals and high-valued fuels is as an effective strategy to achieve a carbon–neutral society [1–10]. However, the CO_2RR process still faces great challenges due to sluggish reaction process and unfavorable competitive hydrogen evolution reaction, thus requiring highly efficient electrocatalysts to obtain desirable products at low overpotentials [11–20]. Though precious metals (e.g., Pd, Au and Ag) have been reported to be efficient in catalyzing the CO_2-to-CO conversion process, the high cost, low stability and limited reserves hampered their practical application [21–26]. Hence, it is of great importance to develop non-precious metals electrocatalysts with low cost, low overpotential and high Faraday efficiency.

Recently, transition metal–nitrogeN-Carbon (M-N-C, M=Ni, Fe and Co) catalysts with atomically dispersed M-N_x sites have demonstrated attractive performance because of their unique electronic structures and near 100% atomic utilization [27–33]. Among them, Ni-N-C has been reported to display superior selectivity for CO_2-to-CO conversion compared to other M-N-C materials [34–37]. In general, the reported Ni-N-C catalysts were often synthesized by directly pyrolyzing metal salts and NC precursors. For instance, Li et al. prepared Ni-N-C via a simple solid-phase pyrolysis of urea and $Ni(NO_3)_2{\cdot}6H_2O$ [38]. The Ni-N-C catalysts could only deliver a CO partial current density (j_{CO}) of –6 mA·cm^{-2} at –0.7 V (vs. RHE). Hou et al. reported single-atom NiN_4 active sites supported by a carbon matrix catalyst, prepared by carbonized the mixture of nickel nitrate and ophenylenediamine, delivering a maximal j_{CO} of –3.5 mA·cm^{-2} at –1.0 V (vs. RHE) [39].

Supplementary Information The online version contains supplementary material available at https://doi.org/10.1007/s12598-022-02247-z.

S.-J. Zheng, H. Cheng*, J. Yu, Q. Bie, J.-D. Chen, F. Wang
Gathering and Transmission Technology Research Institute of Southwest Oil and Gas Field Company of CNPC, Chengdu 610000, China
e-mail: jjsb_ch@163.com

R. Wu, J.-S. Chen*
School of Materials and Energy, University of Electronic Science and Technology of China, Chengdu 611731, China
e-mail: jschen@uestc.edu.cn

D. J. Blackwood
Department of Materials Science and Engineering, National University of Singapore, Singapore 117574, Singapore

Despite great efforts have been made, these Ni-N sites were often randomly dispersed in the carbon host with very limited exposure, resulting in a low utilization of the catalytic centers [40–42]. Therefore, the distribution of Ni-N-C and the nanostructure of the carbon support should be rationally designed to sufficiently expose the active sites, thus improving the catalytic performance toward CO production. The ordered porous structure with a specific surface area not only facilitates the exposure of the active site to the electrolyte, but also ensures the efficient exchange of protons, electrons, carbon dioxide and the target product. However, it is practically very challenging to synthesize porous structures while controlling the formation of Ni-N active sites.

Herein, we report a three-dimensional (3D) ordered porous nitrogen-doped carbon-supported Ni-N_x as effective electrocatalyst for CO_2RR. As illustrated in Scheme 1, the composite catalyst was synthesized by first pyrolyzing a mixture containing polyvinyl pyrrolidone (PVP), nickel-phenanthroline complex and SiO_2 templates, followed by the removal of SiO_2. The porous structures could be easily regulated by tuning the PVP contents which was beneficial to the formation of the ordered honeycomb-like structure, promoting the mass transfer during the catalytic process. The obtained Ni/N-C-100 (Ni/N-C-*X*, where *X* refers to the different amount of PVP added) catalyst achieved a maximal FE_{CO} of 91.1% at − 0.8 V with a large j_{CO} of − 16.2 mA·cm^{-2}. Furthermore, it exhibited a high FE_{CO} over 85% at a broad potential range (− 0.6 to − 0.9 V (vs. RHE)) and maintained high FE_{CO} above 98% after 20 h of reaction at − 0.8 V (vs. RHE). Density functional theory (DFT) calculations showed that the Ni-N_x sites could enhance CO_2RR reaction dynamic process and suppress hydrogen evolution reaction, giving rise to enhanced activity and selectivity.

The morphology of the as-prepared catalysts was first investigated by SEM. Without PVP, a broken frame-like structure was observed for Ni/N-C-0. With the addition of PVP, a honeycomb-like three-dimensional porous structure was formed, signifying that the PVP played a key role in maintaining the integrity of the 3D framework (Figs. 1a–c and S3). Figure 1d shows TEM image of Ni/N-C-100, confirming the interconnected porous structure. The diameter of the pores in Ni/N-C-100 and Ni/N-C-200 was measured to be approximately 180 nm, consistent with the size of silica templates. Moreover, the lattice fringe spacing in the Ni/N-C-100 was 0.34 nm (Fig. S4), corresponding to the (002) plane of graphitized carbon, which indicated high graphitization of the carbon support. Aberration-corrected HAADF-STEM images further illustrated that a large number of isolated bright spots and small patches were identified by red and yellow circles, indicating the presence of both single atoms and clusters in Ni/N-C-100 (Fig. 1e, f). Additionally, the energy-dispersive X-ray spectroscopy (EDX) mapping analysis revealed the homogeneous distribution of C, N, O and Ni in Ni/N-C-100 (Fig. 1g).

X-ray diffraction (XRD) patterns exhibited two broad diffraction peaks at approximately 23° and 43° (Fig. 2a), attributed to the (002) and (100) planes of graphitic carbon, respectively, which confirmed that no Ni-based crystalline phases were formed in all the three samples. As shown in the Raman spectra (Fig. 2b), two distinct peaks at about 1340 (D band) and 1580 cm^{-1} (G band) were observed [27, 36]. Notably, the intensity ratio of D band and G band (I_D/I_G) of Ni/N-C-*X* gradually decreased with the increase in PVP contents, indicating that the introduction of PVP could enhance the graphitization degree of the catalysts. The porous structures of the as-prepared samples were further analyzed by N_2 adsorption–desorption isotherms. Typical type IV isotherms with some hysteresis were observed for all samples (Fig. 2c), indicating mesoporous structure in these catalysts. The corresponding pore size distributions exhibited a sharp peak centered at 0.5 nm (d*V*/d*D* represent pore area), demonstrating the presence of

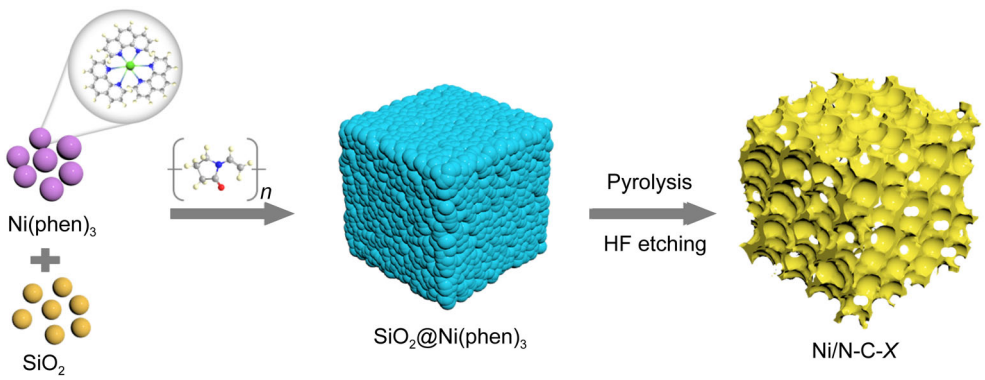

Scheme 1 Schematic illustration of synthesis of Ni/N-C-*X*

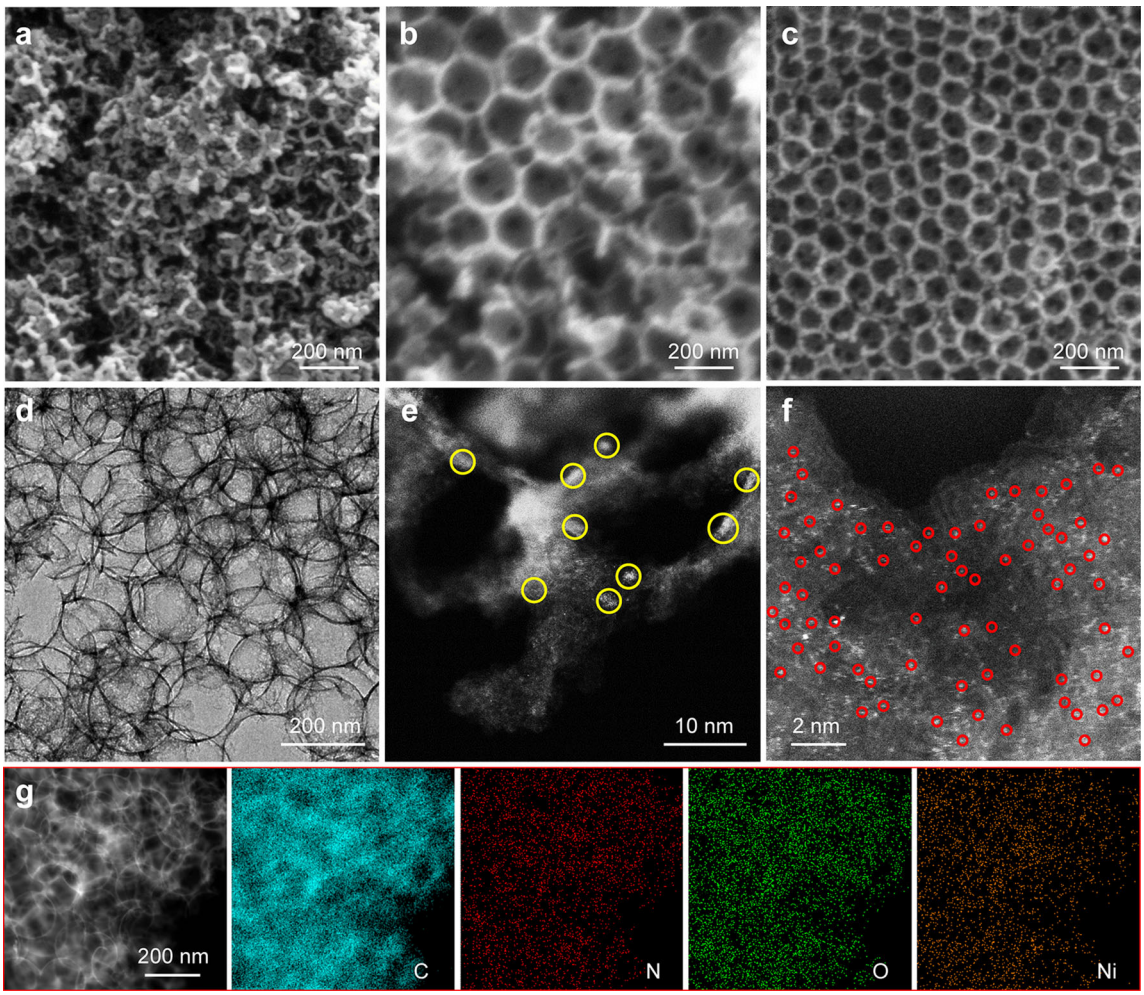

Fig. 1 SEM images of **a** Ni/N-C-0, **b** Ni/N-C-100 and **c** Ni/N-C-200; **d** TEM image and **e, f** HAADF-STEM image of Ni/N-C-100; **g** EDS mapping images of Ni/N-C-100

abundant micropore (Fig. 2d). The specific surface area (S_{BET}) of Ni/N-C-0, Ni/N-C-100 and Ni/N-C-200 was measured to be 807.1, 912.9 and 726.7 $m^2 \cdot g^{-1}$, respectively, signifying that the PVP played a key role in maintaining the integrity of the 3D framework. Benefiting from the high specific surface area and 3D ordered porous structure, the exposure of Ni-N_x sites and mass transfer could be significantly improved for CO_2RR.

X-ray photoelectron spectra (XPS) were further performed to study the elemental composition and chemical state of the as-prepared catalysts. XPS survey spectra of all the three samples showed the existence of C, O, N and Ni (Fig. S5). The high-resolution C 1s spectra of as-prepared catalysts were divided into C–C/C=C ($\sim$ 284.7 eV), C−N ($\sim$ 285.5 eV) and C−O ($\sim$ 288.5 eV), indicating that the N atoms were successfully doped into the carbon framework (Fig. 3a) [43]. Moreover, the binding energies of Ni 2p in Ni/N-C-0, Ni/N-C-100 and Ni/N-C-200 catalysts were reflected by the peak at 855.2 eV, in between metallic Ni^0 (853. eV) and Ni^{2+} (855.7 eV), suggesting that the Ni atoms in these samples are likely to be at a low-valence state (Fig. 3b) [44]. The N 1s spectra of these samples could be fitted into pyridinic-N (398.5 eV), Ni-N_x (399.2 eV), pyrrolic-N (400.8 eV), graphitic-N (401.7 eV) and oxidized-N (404.1 eV). It was believed that the Ni-N_x bond could promote the proton transfer and facilitate the intermediate protonation during the CO_2RR process (Fig. 3c) [3, 39, 45]. Furthermore, the content of each N species is illustrated in Fig. 3d, and the large amount of pyridinic-N in the as-prepared catalysts may favor the activation of CO_2 molecules [46–49]. Furthermore, the presence of Ni-N_x indicates that Ni would directly bind to N rather than forming nanoparticles or clusters, indicating the absence of metallic Ni, which agreed with XRD results.

The CO_2RR electrochemical performance of the three catalysts was first investigated by linear sweep voltammetry (LSV). As depicted in Figs. 4a and S6, all samples showed a higher current response in CO_2-saturated 0.5 $mol \cdot L^{-1}$ $KHCO_3$ electrolyte than in the Ar-saturated counterpart, suggesting that the Ni/N-C catalysts were

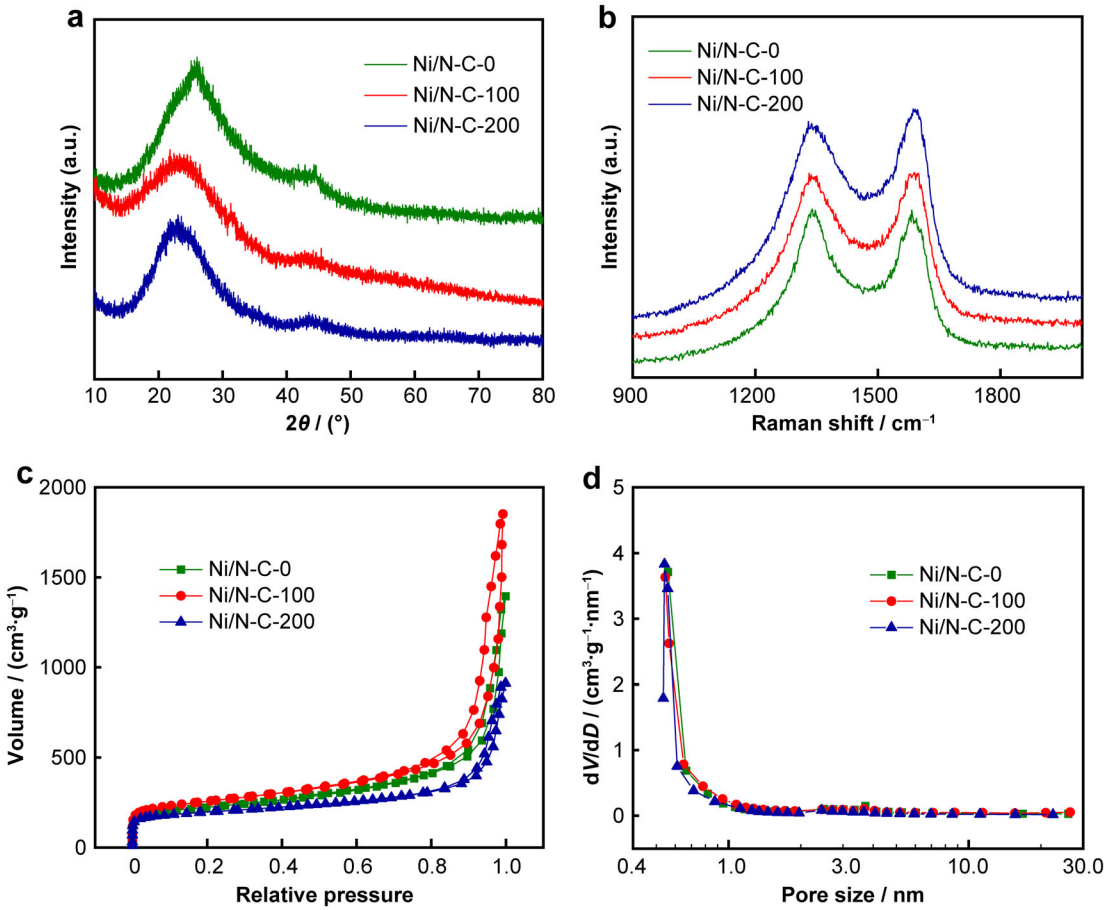

Fig. 2 **a** XRD patterns, **b** Raman spectra, **c** N_2 adsorption–desorption isotherms and **d** pore size distribution of Ni/N-C-0, Ni/N-C-100, Ni/N-C-200

active for CO_2RR. Both Ni/N-C-0 and Ni/N-C-100 showed much larger j than Ni/N-C-200 at all applied potentials. Specifically, the j of Ni/N-C-100 reached as high as 40 mA·cm^{-2} at –1.0 V (vs. RHE), showing excellent catalytic activity. Next, controlled potential electrolysis at various potentials was carried out in an H-type cell with a three-electrode system to further evaluate the catalytic activity and selectivity in CO_2RR. Nuclear magnetic resonance (NMR) spectroscopy and online gas chromatography (GC) were used to analyze the gaseous and liquid products, respectively, and only CO and H_2 were detected as the gaseous products (Fig. S7). As depicted in Fig. 4b, the cathodic j_{total} of Ni/N-C-100 gradually increased as the potential increased from –0.6 to –1.0 V (vs. RHE) and remained unchanged after 1800 s, reflecting enhanced electrochemical stability at these applied potentials (Fig. S8). The j could reach about 30 mA·cm^{-2} at –1.0 V (vs. RHE) during the long-term test for 30 min. By comparing the FE_{CO} of Ni/N-C-0, Ni/N-C-100, and Ni/N-C-200 catalysts at various potentials, it could be found that the FE_{CO} of Ni/N-C-100 remained above 85% ranged from –0.6 to –0.9 V (vs. RHE) (Figs. 4c and S9). Notably, the FE_{CO} of Ni/N-C-100 was up to 91.1% at –0.8 V (vs. RHE), while that of Ni/N-C-0 and Ni/N-C-200 was 90.1% and 86.9%, respectively. To get more insight of the active site, the KSCN poisoning experiment was conducted. As shown in Fig. S10, a significant decrease in CO Faradaic efficiency was observed for Ni/N-C-100, confirming the catalytic role of Ni-N_x active site. Moreover, the j_{CO} of Ni/N-C-100 was calculated to be 14.34 mA·cm^{-2} at –0.8 V (vs. RHE), which was 3.7 and 3.1 times higher than those of Ni/N-C-0 (3.85 mA·cm^{-2}) and Ni/N-C-200 (4.6 mA·cm^{-2}), respectively (Fig. 4d), further confirming the advantage of the hierarchical porous structure.

To further reveal the origin of the superior performance, the electrochemical active surface area (ECSA) of the as-prepared samples was measured. The double-layer capacitance (C_{dl}) was first determined by the cyclic voltammetry (CV) curves at different scan rates (Figs. 4e and S11), where the value of C_{dl} was proportional to the ECSA of the electrocatalyst. It is thus apparent that Ni/N-C-100 had a higher ECSA than the other two counterparts, resulting in the highest j_{CO}. Additionally, ECSA-normalized current density of all the three samples is provided in Fig. S12.

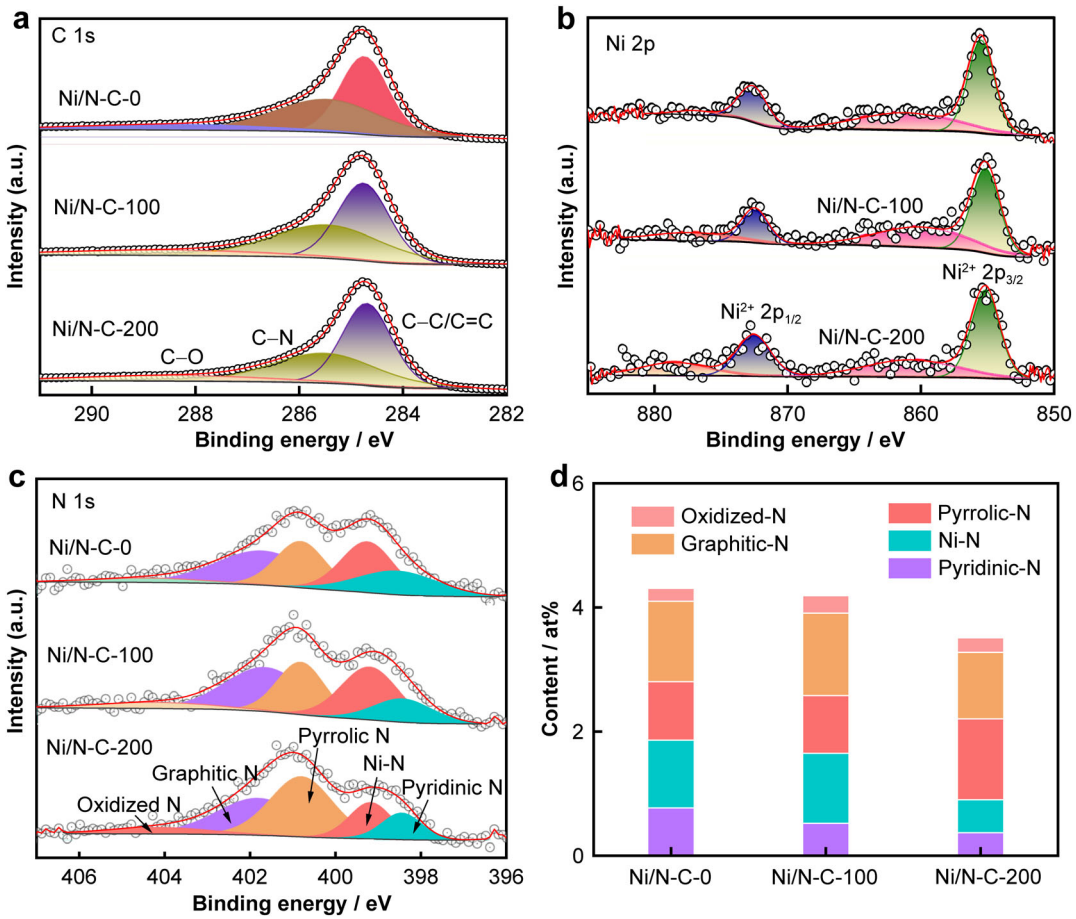

Fig. 3 High-resolution XPS spectra of Ni/N-C-0, Ni/N-C-100, Ni/N-C-200: **a** C 1s, **b** Ni 2p, and **c** N 1s; **d** atomic content of pyridine–N, Ni-N, pyrrole-N, graphitic-N and oxide-N for three samples

Notably, Ni/N-C-100 possessed a lower specific CO current density than Ni/N-C-0. The porous structure is beneficial to the exposure of active sites and the penetration of the electrolyte, resulting in a larger current density of Ni/N-C-100 in CO_2RR. The long-term electrolysis of Ni/N-C-100 at the potential of –0.8 V (vs. RHE) (Fig. 4f) indicated that 90% of its initial FE_{CO} could be retained without any significant change in current density after 20 h of continuous operation, and its 3D ordered porous structure (Fig. S13) and XRD pattern (Fig. S14) demonstrated almost no change before and after the long-term test, reflecting its high robustness.

To gain a deeper understanding of the superior CO_2RR electrochemical performance of Ni/N-C-100, DFT calculation was performed. Based on XRD and HAADF-STEM results, the modeling for cluster/Ni-N-C was built by arranging a Ni cluster onto the surface of Ni-N-C. For comparison, a Ni cluster and Ni-N-C model were also constructed (Fig. S15). As shown in Fig. 5a, the first step of CO_2 to form COOH* intermediates was the rate-limiting step (RDS) for cluster/Ni-N-C and Ni-N-C, and the free-energy change (ΔG) for this step on cluster/Ni-N-C (0.99 eV) was significantly smaller than that on Ni-N-C (1.62 eV), indicating enhanced reaction dynamic process [27, 29]. Although the Ni cluster exhibited a lower free-energy change for the formation of *COOH intermediates (− 0.38 eV) than cluster/Ni-N-C (1.46 eV), the CO desorption energy on Ni cluster was much higher than that on cluster/Ni-N-C, which indicated that CO molecule would be trapped on the Ni cluster surface, resulting in a sluggish reaction dynamic process [33, 44]. Furthermore, cluster/Ni-N-C possessed a higher H* adsorption energy (0.81 eV) than pure Ni cluster (− 0.56 eV), demonstrating that HER view was well inhibited on cluster/Ni-N-C (Fig. S16). Moreover, the structural evolution of active site on cluster/Ni-N-C is shown in Fig. 5b, visually reflecting that CO_2RR catalytic process. In addition, Fig. 5c exhibits the charge density difference of the adsorbed COOH* intermediates on cluster/Ni-N-C, Ni cluster and Ni-N-C. The electron transfer between adsorbed COOH* and cluster/Ni-N-C was much stronger than that with Ni-N-C, reflecting enhanced ability toward COOH* formation for cluster/Ni-N-C.

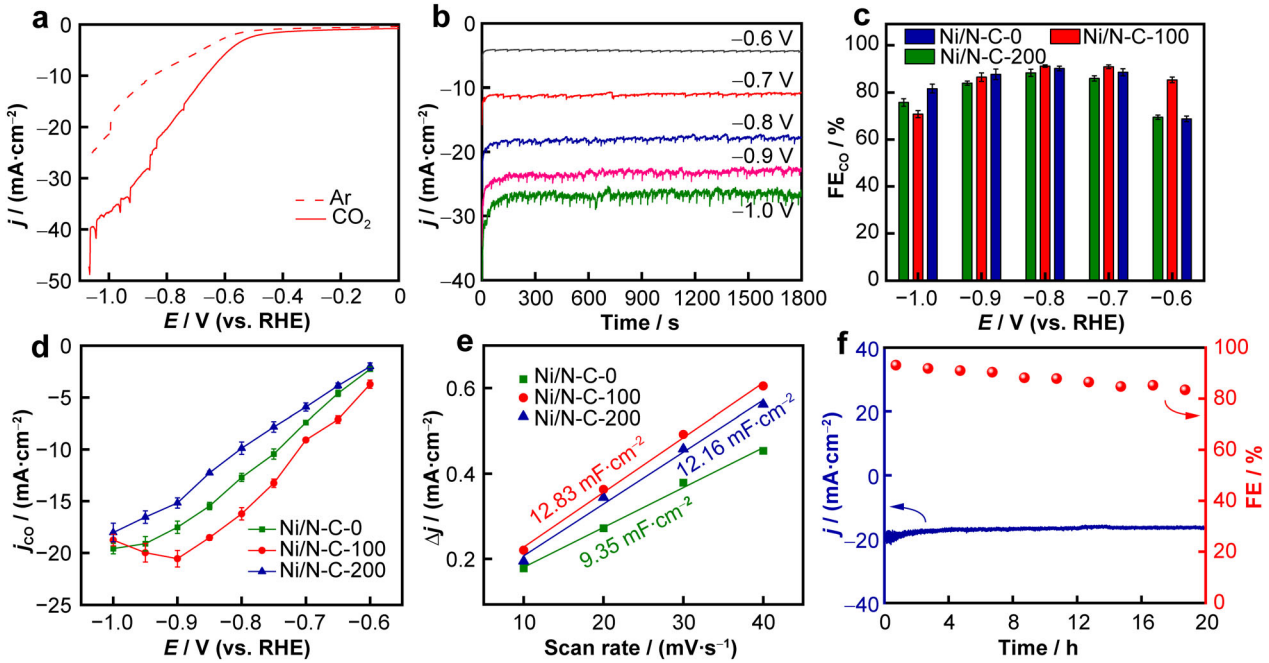

Fig. 4 **a** LSV curves for Ni/N-C-100 in 0.5 mol·L^{-1} CO_2-saturated $KHCO_3$ electrolyte; **b** chronoamperometric (*i-t*) curves of Ni/N-C-100 at different potentials; **c** FE_{CO} at different potentials; **d** j_{co} for all samples at various potentials; **e** electrochemical double layer capacitance measurements for Ni/N-C-0, Ni/N-C-100, Ni/N-C-200; **f** long-term stability of Ni/N-C-100 at –0.8 V (vs. RHE)

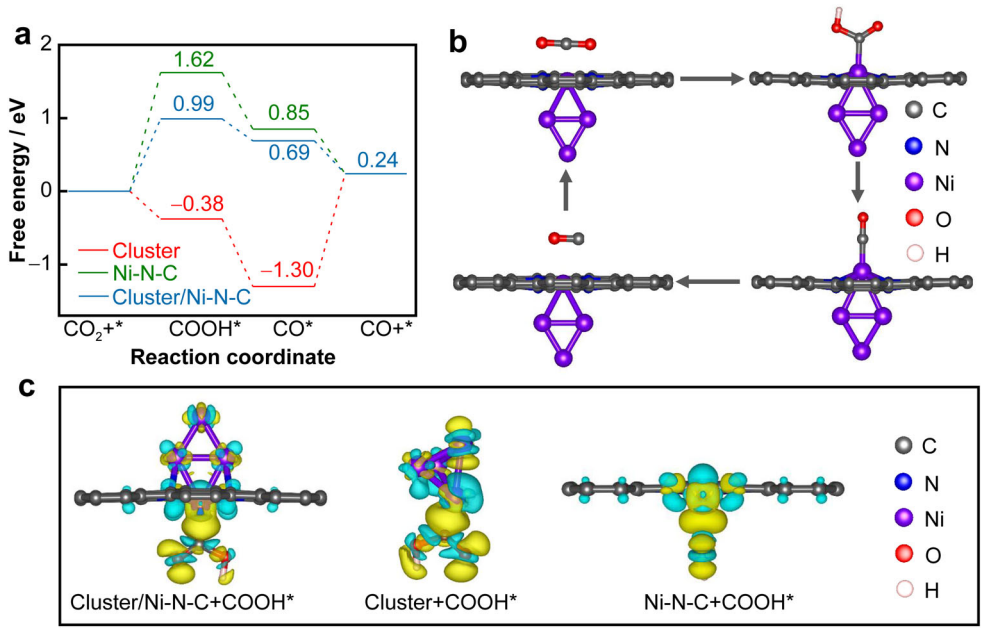

Fig. 5 **a** Free-energy diagram of CO_2 electroreduction to CO over cluster/Ni-N-C and Ni cluster; **b** structural evolution of active site for cluster/Ni-N-C in CO_2RR process; **c** charge density difference of cluster/Ni-N-C, Ni cluster and Ni-N-C with COOH* adsorption from 3-dimensional

In summary, utilizing SiO_2 as the hard template and PVP as a structure directing agent, highly ordered honeycomb-like 3D porous carbon framework loaded with atomically dispersed Ni-N_x species was constructed. When used for CO_2RR, the as-prepared Ni/N-C-100 catalyst exhibited a high FECO of 91.1% at –0.8 V (vs. RHE) with j_{CO} of –16.2 mA·cm^{-2}, and robust stability after a 20-h long-term electrolysis. DFT calculations have demonstrated that the Ni-N_x active sites were beneficial to the formation of CO key intermediates and suppress hydrogen

evolution reaction, giving rise to enhanced activity and selectivity. This work developed a facile method for the preparation of high-performance Ni single-atom electrocatalysts, which can also be applied to a widespread range of electrochemical applications.

Acknowledgements This study was financially supported by the National Key R&D Program of China (No. 2021YFB2401902).

Declarations

Conflict of interests The authors declare that they have no conflict of interest.

References

[1] Liu HF, Xia J, Zhang N, Cheng H, Bi WT, Zu XL, Chu WS, Wu HA, Wu CZ, Xie Y. Solid-liquid phase transition induced electrocatalytic switching from hydrogen evolution to highly selective CO_2 reduction. Nat Catal. 2021;4(4):202. https://doi.org/10.1038/s41929-021-00608-y.

[2] Li JJ, Zhang ZC. K^+-enhanced electrocatalytic CO_2 reduction to multicarbon products in strong acid. Rare Met. 2022;41(3):723. https://doi.org/10.1007/s12598-021-01862-6.

[3] Pei J, Wang T, Sui R, Zhang X, Zhou D, Qin F, Zhao X, Liu Q, Yan W, Dong J, Zheng L, Li A, Mao J, Zhu W, Chen W, Zhuang Z. N-Bridged Co–N–Ni: new bimetallic sites for promoting electrochemical CO_2 reduction. Energy Environ Sci. 2021;14(5):3019. https://doi.org/10.1039/D0EE03947K.

[4] Liu K, Wang J, Shi M, Yan J, Jiang Q. Simultaneous achieving of high faradaic efficiency and CO partial current density for CO_2 reduction via robust, noble-metal-free Zn nanosheets with favorable adsorption energy. Adv Energy Mater. 2019;9(21):1900276. https://doi.org/10.1002/aenm.201900276.

[5] Li Q, Wang YC, Zeng J, Zhao X, Chen C, Wu QM, Chen LM, Chen ZY, Lei YP. Bimetallic chalcogenides for electrocatalytic CO_2 reduction. Rare Met. 2021;40(12):3442. https://doi.org/10.1007/s12598-021-01772-7

[6] Yang H, Huang Y, Deng J, Wu Y, Han N, Zha C, Li L, Li Y. Selective electrocatalytic CO_2 reduction enabled by SnO_2 nanoclusters. J Energy Chem. 2019;37:93. https://doi.org/10.1016/j.jechem.2018.12.004.

[7] Liu XX, Chen C, He Q, Kong Q, Blackwood DJ, Li NW, Yu L, Chen JS. Self-supported transition metal-based nanoarrays for efficient energy storage. Chem Rec. 2022. https://doi.org/10.1002/tcr.202100294.

[8] Yu X, Shao M, Yang X, Li C, Li T, Li D, Wang R, Yin L. A high-performance potassium-ion capacitor based on a porous carbon cathode originated from the Aldol reaction product. Chin Chem Lett. 2020;31(9):2215. https://doi.org/10.1016/j.cclet.2019.11.012.

[9] Abbas M, Sial MAZG. New horizon in stabilization of single atoms on metal-oxide supports for CO_2 reduction. Nano Mater Sci. 2021;3(4):368. https://doi.org/10.1016/j.nanoms.2021.07.009.

[10] Yang H, Liu Y, Liu X, Wang X, Tian H, Waterhouse GIN, Kruger PE, Telfer SG, Ma S. Large-scale synthesis of N-doped carbon capsules supporting atomically dispersed iron for efficient oxygen reduction reaction electrocatalysis. eScience. 2022;2(2):227. https://doi.org/10.1016/j.esci.2022.02.005.

[11] Zhang Y, Hu T, Ke C, Han F, Xiao W, Yang X. Ru nanoclusters confined on α/β cobalt hydroxide nanosheets as efficient bifunctional oxygen electrocatalysts for Zn-air batteries. Inorg Chem Front. 2022. https://doi.org/10.1039/d2qi01585d.

[12] Shen S, Han C, Wang B, Wang Y. Engineering d-band center of nickel in nickel@nitrogen-doped carbon nanotubes array for electrochemical reduction of CO_2 to CO and ZN-CO_2 batteries. Chin Chem Lett. 2021;33(8):3721. https://doi.org/10.1016/j.cclet.2021.10.063.

[13] Cui Y, Zhang Y, Cao Z, Gu J, Du Z, Li B, Yang S. A perspective on high-entropy two-dimensional materials. SusMat. 2022;2(1):65. https://doi.org/10.1002/sus2.47.

[14] Zhang S, Gao XT, Hou PF, Zhang TR, Kang P. Nitrogen-doped Zn–Ni oxide for electrochemical reduction of carbon dioxide in sea water. Rare Met. 2021;40(11):3117. https://doi.org/10.1007/s12598-021-01774-5.

[15] Yin C, Li Q, Zheng J, Ni Y, Wu H, Kjøniksen AL, Liu C, Lei Y, Zhang Y. Progress in regulating electronic structure strategies on Cu-based bimetallic catalysts for CO_2 reduction reaction. Adv Powder Mater. 2022;1(4):100055. https://doi.org/10.1016/j.apmate.2022.100055.

[16] Du J, Liu L, Yu Y, Zhang Y, Chen A. "Dissolution-reassembly" for N-doped hollow micro/meso-carbon spheres with high supercapacitor performance. Chin Chem Lett. 2019;30(7):1423. https://doi.org/10.1016/j.cclet.2019.03.004.

[17] Zeng J, Bejtka K, Ju W, Castellino M, Chiodoni A, Sacco A, Farkhondehfal MA, Hernández S, Rentsch D, Battaglia C, Pirri CF. Advanced Cu-Sn foam for selectively converting CO_2 to CO in aqueous solution. Appl Catal B Environ. 2018;236:475. https://doi.org/10.1016/j.apcatb.2018.05.056.

[18] Chen Y, Chen K, Fu J, Yamaguchi A, Li H, Pan H, Hu J, Miyauchi M, Liu M. Recent advances in the utilization of copper sulfide compounds for electrochemical CO_2 reduction. Nano Mater Sci. 2020;2(3):235. https://doi.org/10.1016/j.nanoms.2019.10.006.

[19] Geng Z, Kong X, Chen W, Su H, Liu Y, Cai F, Wang G, Zeng J. Oxygen vacancies in ZnO nanosheets enhance CO_2 electrochemical reduction to CO. Angew Chem Int Ed. 2018;57(21):6054. https://doi.org/10.1002/anie.201711255.

[20] Hu C, Bai S, Gao L, Liang S, Yang J, Cheng SD, Mi SB, Qiu J. Porosity-induced high selectivity for CO_2 electroreduction to CO on Fe-doped ZIF-derived carbon catalysts. ACS Catal. 2019;9(12):11579. https://doi.org/10.1021/acscatal.9b03175.

[21] Yang CH, Nosheen F, Zhang ZC. Recent progress in structural modulation of metal nanomaterials for electrocatalytic CO_2 reduction. Rare Met. 2021;40(6):1412. https://doi.org/10.1007/s12598-020-01600-4.

[22] Yan D, Zhang L, Shen L, Hu R, Xiao W, Yang X. Pd nanoparticles enbedded in N-enriched MOF-derived architectures for efficient oxygen reduction reaction in alkaline media. Green Energy Environ. 2022. https://doi.org/10.1016/j.gee.2022.01.011.

[23] Zhao L, Wu R, Wang J, Li Z, Wei X, Chen JS, Chen Y. Synthesis of noble metal-based intermetallic electrocatalysts by space-confined pyrolysis: recent progress and future perspective. J Energy Chem. 2021;60:61. https://doi.org/10.1016/j.jechem.2020.12.021.

[24] Wang JJ, Li XP, Cui BF, Zhang Z, Hu XF, Ding J, Deng YD, Han XP, Hu WB. A review of non-noble metal-based electrocatalysts for CO_2 lectroreduction. Rare Met. 2021;40(11):3019. https://doi.org/10.1007/s12598-021-01736-x.

[25] Jia Y, Li F, Fan K, Sun L. Cu-based bimetallic electrocatalysts for CO_2 reduction. Adv Powder Mater. 2021;1(1):100012. https://doi.org/10.1016/j.apmate.2021.10.003.

[26] Wang J, Zhu Z, Wei X, Li Z, Chen JS, Wu R, Wei Z. Hydrogen-mediated synthesis of 3D hierarchical porous zinc catalyst for CO_2 electroreduction with high current density. J Phys Chem

C. 2021;125(43):23784. https://doi.org/10.1021/acs.jpcc.1c07498.
[27] Li Z, Wu R, Xiao S, Yang Y, Lai L, Chen JS, Chen Y. Axial chlorine coordinated iron-nitrogen-carbon single-atom catalysts for efficient electrochemical CO_2 reduction. Chem Eng J. 2022;430:132882. https://doi.org/10.1016/j.cej.2021.132882.
[28] Zhang Y, Qi K, Li J, Karamoko BA, Lajaunie L, Godiard F, Oliviero E, Cui X, Wang Y, Zhang Y, Wu H, Wang W, Voiry D. 26% cm^{-2} single-pass CO_2-to-CO conversion using Ni single atoms supported on ultra-thin carbon nanosheets in a flow electrolyzer. ACS Catal. 2021;11(20):12701. https://doi.org/10.1021/acscatal.1c03231.
[29] Wei X, Xiao S, Wu R, Zhu Z, Zhao L, Li Z, Wang J, Chen JS, Wei Z. Activating COOH* intermediate by Ni/$Ni_3ZnC_{0.7}$ heterostructure in porous N-doped carbon nanofibers for boosting CO_2 electroreduction. Appl Catal B: Environ. 2022;302:120861. https://doi.org/10.1016/j.apcatb.2021.120861.
[30] Li Z, Wu R, Zhao L, Li P, Wei X, Wang J, Chen JS, Zhang T. Metal-support interactions in designing noble metal-based catalysts for electrochemical CO_2 reduction: recent advances and future perspectives. Nano Res. 2021;14(11):3795. https://doi.org/10.1007/s12274-021-3363-6.
[31] Wang C, Liu Y, Ren H, Guan Q, Chou S, Li W. Diminishing the uncoordinated N species in Co–N-C catalysts toward highly efficient electrochemical CO_2 reduction. ACS Catal. 2022;12(4):2513. https://doi.org/10.1021/acscatal.1c05029.
[32] Duarte M, Daems N, Hereijgers J, Arenas-Esteban D, Bals S, Breugelmans T. Enhanced CO electroreduction with metal-nitrogen-doped carbons in a continuous flow reactor. J CO_2 Utili. 2021;50:101583. https://doi.org/10.1016/j.jcou.2021.101583.
[33] Zhu Z, Li Z, Wang J, Li R, Chen H, Li Y, Chen JS, Wu R, Wei Z. Improving NiN_X and pyridinic N active sites with space-confined pyrolysis for effective CO_2 electroreduction. eScience. 2022;2:445. https://doi.org/10.1016/j.esci.2022.05.002.
[34] Möller T, Ju W, Bagger A, Wang X, Luo F, Ngo TT, Varela AS, Rossmeisl J, Strasser P. Efficient CO_2 to CO electrolysis on solid Ni-N-C catalysts at industrial current densities. Energy Environ Sci. 2019;12(2):640. https://doi.org/10.1039/c8ee02662a.
[35] Zhang M, Wu TS, Hong S, Fan Q, Soo YL, Masa J, Qiu J, Sun Z. Efficient electrochemical reduction of CO_2 by Ni-N-C catalysts with tunable performance. ACS Sustain Chem Eng. 2019;7(17):15030. https://doi.org/10.1021/acssuschemeng.9b03502.
[36] Zhu Z, Li Z, Wei X, Wang J, Xiao S, Li R, Wu R, Chen JS. Achieving efficient electroreduction of CO_2 to CO in a wide potential window by encapsulating Ni nanoparticles in N-doped carbon nanotubes. Carbon. 2021;185:9. https://doi.org/10.1016/j.carbon.2021.08.072.
[37] Li C, Ju W, Vijay S, Timoshenko J, Mou K, Cullen DA, Yang J, Wang X, Pachfule P, Bruckner S, Jeon HS, Haase FT, Tsang SC, Rettenmaier C, Chan K, Cuenya BR, Thomas A, Strasser P. Covalent organic framework (COF) derived Ni-N-C catalysts for electrochemical CO_2 reduction: unraveling fundamental kinetic and structural parameters of the active sites. Angew Chem Int Ed. 2022;61(15):e202114707. https://doi.org/10.1002/anie.202114707.
[38] Pan F, Deng W, Justiniano C, Li Y. Identification of champion transition metals centers in metal and nitrogen-codoped carbon catalysts for CO_2 reduction. Appl Catal B Environ. 2018;226:463. https://doi.org/10.1016/j.apcatb.2018.01.001.
[39] Wang X, Sang X, Dong CL, Yao S, Shuai L, Lu J, Yang B, Li Z, Lei L, Qiu M, Dai L, Hou Y. Proton capture strategy for enhancing electrochemical CO_2 reduction on atomically dispersed metal-nitrogen active sites. Angew Chem Int Ed. 2021;60(21):11959. https://doi.org/10.1002/anie.202100011.
[40] Wang C, Hu X, Hu X, Liu X, Guan Q, Hao R, Liu Y, Li W. Typical transition metal single-atom catalysts with a metal--pyridine N structure for efficient CO_2 electroreduction. Appl Catal B Environ. 2021;296:120331. https://doi.org/10.1016/j.apcatb.2021.120331.
[41] Guo H, Si DH, Zhu HJ, Li QX, Huang YB, Cao R. Ni single-atom sites supported on carbon aerogel for highly efficient electroreduction of carbon dioxide with industrial current densities. eScience. 2022;2(3):295. https://doi.org/10.1016/j.esci.2022.03.007.
[42] Leverett J, Yuwono JA, Kumar P, Tran-Phu T, Qu J, Cairney J, Wang X, Simonov AN, Hocking RK, Johannessen B, Dai L, Daiyan R, Amal R. Impurity tolerance of unsaturated Ni-N-C active sites for practical electrochemical CO_2 reduction. ACS Energy Lett. 2022;7(3):920. https://doi.org/10.1021/acsenergylett.1c02711.
[43] Yang M, Huang M, Li Y, Feng Z, Huang Y, Chen H, Xu Z, Liu H, Wang Y. Printing assembly of flexible devices with oxidation stable MXene for high performance humidity sensing applications. Sens Actuators B Chem. 2022;364:131867. https://doi.org/10.1016/j.snb.2022.131867.
[44] Wang J, Li Z, Zhu Z, Jiang J, Li Y, Chen J, Niu X, Chen JS, Wu R. Tailoring the interactions of heterostructured Ni_4N/$Ni_3ZnC_{0.7}$ for efficient CO_2 electroreduction. J Energy Chem. 2022;75:1. https://doi.org/10.1016/j.jechem.2022.07.037.
[45] Zheng W, Wang Y, Shuai L, Wang X, He F, Lei C, Li Z, Yang B, Lei L, Yuan C, Qiu M, Hou Y, Feng X. Highly boosted reaction kinetics in carbon dioxide electroreduction by surface-introduced electronegative dopants. Adv Funct Mater. 2021;31(15):2008146. https://doi.org/10.1002/adfm.202008146.
[46] Lu Q, Chen C, Di Q, Liu W, Sun X, Tuo Y, Zhou Y, Pan Y, Feng X, Li L, Chen D, Zhang J. Dual role of pyridinic-N doping in carbon-coated Ni nanoparticles for highly efficient electrochemical CO_2 reduction to CO over a wide potential range. ACS Catal. 2022;12(2):1364. https://doi.org/10.1021/acscatal.1c04825.
[47] Li H, Xiao N, Hao M, Song X, Wang Y, Ji Y, Liu C, Li C, Guo Z, Zhang F, Qiu J. Efficient CO_2 electroreduction over pyridinic-N active sites highly exposed on wrinkled porous carbon nanosheets. Chem Eng J. 2018;351:613. https://doi.org/10.1016/j.cej.2018.06.077.
[48] Li Q, Zhu W, Fu J, Zhang H, Wu G, Sun S. Controlled assembly of Cu nanoparticles on pyridinic-N rich graphene for electrochemical reduction of CO_2 to ethylene. Nano Energy. 2016;24:1. https://doi.org/10.1016/j.nanoen.2016.03.024.
[49] Ning H, Guo D, Wang X, Tan Z, Wang W, Yang Z, Li L, Zhao Q, Hao J, Wu M. Efficient CO_2 electroreduction over N-doped hieratically porous carbon derived from petroleum pitch. J Energy Chem. 2021;56:113. https://doi.org/10.1016/j.jechem.2020.07.049.